International Journal of Heat and Mass Transfer 52 (2009) 3857–3868

Contents lists available at ScienceDirect

International Journal of Heat and Mass Transfer

journal homepage: www.elsevier.com/locate/ijhmt

Prevention of fouling and scaling in stationary and circulating liquid–solid fluidized bed heat exchangers: Particle impact measurements and analysis

P. Pronk *, C.A. Infante Ferreira, G.J. Witkamp

Process & Energy Laboratory, Delft University of Technology, Leeghwaterstraat 44, 2628 CA Delft, The Netherlands

ARTICLE INFO

Article history:
Received 14 February 2006
Accepted 26 September 2008
Available online 7 April 2009

Keywords:
Fouling
Scaling
Collision mechanics
Liquid–solid fluidized bed
Heat exchanger

ABSTRACT

Fluidized particles in liquid–solid fluidized bed heat exchangers are able to remove deposits from the walls and thus to prevent fouling or scaling. This fouling prevention ability is believed to depend strongly on the frequency and force of particle–wall collisions. This paper presents piezoelectric measurements of impacts on the wall in both stationary and circulating fluidized beds of various particle sizes and bed voidages. Two types of impacts were measured, namely by collisions of particles on the sensor and by liquid pressure fronts induced by particle–particle collisions close to the sensor. The characteristics of both impact types are used to analyze the total impulse and energy exerted by impacts on the wall for various fluidized beds.

1. Introduction

Many industrial heat transfer processes suffer from the deposition of solids on heat exchanger walls, often referred to as fouling, scaling, encrustation or incrustation [1–3]. The deposits can either be formed by suspended particles that stick to the wall or by crystalline material that crystallizes on the wall due to the local supersaturation. For both cases, fouling reduces overall heat transfer coefficients significantly and increases pressure drop, and is therefore one of the major problems for process industries. In order to avoid excessive fouling, heat exchangers are periodically cleaned requiring costly maintenance stops. Another possibility is to equip heat exchangers with fouling control techniques, such as expensive mechanical scrapers that continuously remove deposits from the walls [4].

A promising alternative to these conventional fouling control techniques is the liquid–solid fluidized bed heat exchanger, which requires less investment and maintenance costs [5,6]. This heat exchanger type usually consists of a vertical shell-and-tube configuration with a fluidized bed of steel, glass or ceramic particles in the tubes (see Fig. 1). The fluidized particles continuously impact on the walls and are therefore able to keep them free of deposits. Secondary advantages of fluidized beds are the enhanced heat and mass transfer coefficients, which can be up to eight times higher than for the case without particles [7,8]. Typical applications are found in various parts of industry where severe fouling occurs, such as desalination plants, geothermal plants, paper industry, refineries and waste water treatment [9,10]. A relatively new application is the crystallization of ice suspensions from aqueous solutions [11,12].

The ability of fluidized beds to remove deposits from heat exchanger walls and the enhancement of heat and mass transfer rates are attributed to particle collisions with the wall. Due to their importance, particle–wall collisions and individual particle movements have been experimentally studied for both stationary and circulating fluidized beds. Individual particle velocities were mainly measured by using visual observation techniques with tracer particles [13–16], while piezoelectric sensors were used to measure particle–wall collisions [17–23]. Although the latter measurements were successful, expressions for collision frequencies and particles impact velocities as a function of bed voidage, particle size and circulation rate are lacking. Furthermore, it is not clear how particle–wall collisions are related to the removal of deposits. The most plausible options are that the removal is proportional to the total impulse generated by the particles on the wall, also referred to as particle pressure, or to the total kinetic energy of the particles that hit the wall [18,23,24].

The first aim of this paper is to characterize both frequency and impact velocities of particle–wall collisions in liquid–solid fluidized bed heat exchangers. For this purpose, a piezoelectric sensor was used to measure collisions in both stationary and circulating fluidized beds at various bed voidages with stainless steel particles of 2, 3 or 4 mm. The second aim is to use these collision characteristics to formulate expressions for the total kinetic energy of particles that hit the wall and the total impulse exerted by the particles on the wall as a function of bed voidage, particle size and circulation rate.

* Corresponding author. Tel.: +31 251 494830; fax: +31 15 2782460.
E-mail address: p.pronk@tudelft.nl (P. Pronk).

0017-9310/$ - see front matter © 2009 Published by Elsevier Ltd.
doi:10.1016/j.ijheatmasstransfer.2008.09.043

Nomenclature

a	parameter in Eq. (20), N m^{-2}
A	area, m^2
b	parameter in Eq. (20), N$^{1/2}$ m^{-1} s^{-1}
c	speed of sound, m s^{-1}
d_p	equivalent particle diameter ($6^{1/3}\pi^{-1/3}V_p^{1/3}$), m
e_{p-w}	energy of single particle–wall collision, J
e_{lpf}	energy of single pressure front per m^2, J m^{-2}
E	total energy of particles and pressure fronts hitting the wall, W m^{-2}
E_{p-w}	total kinetic energy of particles hitting the wall, W m^{-2}
E_{lpf}	total energy of pressure fronts reaching the wall, W m^{-2}
E	modulus of elasticity, N m^{-2}
f_A	particle–wall collision frequency, m^{-2} s^{-1}
f_V	particle–particle collision frequency, m^{-3} s^{-1}
f	function
F_{max}	maximum force, N
g	gravity, m s^{-2}
g_0	Gidaspow parameter, defined in Eq. (11)
$g_{0,adj}$	adjusted Gidaspow parameter, defined in Eq. (12)
h	height, m
j_{p-w}	impulse of single particle–wall collision, N s
j_{lpf}	impulse of single pressure front per unit of area, N s m^{-2}
J	total impulse exerted by particles and pressure fronts on the wall, N s m^{-2} s^{-1}
J_{p-w}	total impulse exerted by particles on the wall, N s m^{-2} s^{-1}
J_{lpf}	total impulse exerted by pressure fronts on the wall, N s m^{-2} s^{-1}
l	dimensionless length ($r\ d_p^{-1}$)
m	mass, kg
$\dot{m}$	mass flow rate, kg s^{-1}
p	pressure, Pa
p_{max}	maximum pressure, Pa
Δp	pressure drop, Pa
r	distance, m
t	time, s
T	temperature, °C
u_s	superficial liquid velocity
v_{slip}	slip velocity, m s^{-1}
v_p	particle velocity, m s^{-1}
v_r	radial particle velocity, m s^{-1}
v_z	net upward particle velocity, m s^{-1}
V	volume, m^3
$\dot{V}$	volume flow rate, m^3 s^{-1}
x	parameter (p_{max}/a)
y_A	number density of particle–wall collisions, m^{-3}
y_j	number density of liquid pressure fronts at a point at the wall, s^{-1} Pa^{-1}
y_V	number density of particle–particle collisions, m^{-4} or m^{-3} s^{-1} Pa^{-1}

Greek letters

Γ	gamma function
ε	bed voidage
θ	angle in polar coordinates
ρ	density, kg m^{-3}
τ	contact time, s
υ	Poisson's ratio
φ	angle in polar coordinates

Subscripts

avg	average
cfb	circulating fluidized bed
liq	liquid
liq–w	liquid–wall
lpf	liquid pressure front
fr	friction
p	particle
pb	packed bed
p–p	particle–particle
p–w	particle–wall
s	sensor
sfb	stationary fluidized bed

Abbreviations

CFB	circulating fluidized bed
CFD	computational fluid dynamics
SFB	stationary fluidized bed

2. Experimental set-up

2.1. Single-tube fluidized bed heat exchanger

The experiments were carried out with a single-tube fluidized bed heat exchanger as shown in Fig. 2. The heat exchanger consisted of two stainless steel tube-in-tube heat exchangers connected by a stainless steel tube. The internal diameter of the inner tubes and the connection tube measured 42.7 mm and the total length of the heat exchanger was 4.88 m. The fluidized bed consisted of tap water and cylindrical stainless steel particles of approximately 2, 3 or 4 mm in both height and diameter with a density of 7900 kg m^{-3}. The average equivalent particle diameters were determined from weight measurements and measured 2.1, 3.2 and 4.3 mm, respectively.

The fluidized bed was cooled by a 34 wt% potassium formate solution flowing counter currently through the annuli. The inlet temperature of the coolant was 17 °C, while a electrical heater in the water tank controlled the water inlet temperature at 20 °C. The fluidized bed was operated in both stationary and circulating mode. In the latter mode, particles were dragged out at the top of the heat exchanger and were recirculated to its inlet via a downcomer tube with an internal diameter of 34 mm. A part of the flow from the water tank, named control flow, was used to transport particles from the bottom of the downcomer to the inlet of the fluidized bed.

In order to determine the bed voidage in the fluidized bed, pressures were measured at the top and bottom of the heat exchanger. The bed voidage was deduced from the measured pressure drop in the fluidized bed which consists of a hydrostatic term, a term for the liquid–wall friction and a term for the particle–wall friction [16]:

$$\Delta p = gh(\varepsilon\rho_{liq} + (1-\varepsilon)\rho_p) + \Delta p_{fr,liq-w} + \Delta p_{fr,p-w} \quad (1)$$

The pressure drop by friction between the liquid and the wall was determined from experiments without particles. The friction between particles and wall was neglected.

2.2. Measurement of particle collisions

A piezoelectric sensor of type KISTLER 601A with a diameter of 5.5 mm was mounted in the connection tube such that the membrane of the sensor smoothly followed the inner surface of the tube (see Fig. 2). The duration of collisions was typically in the order of

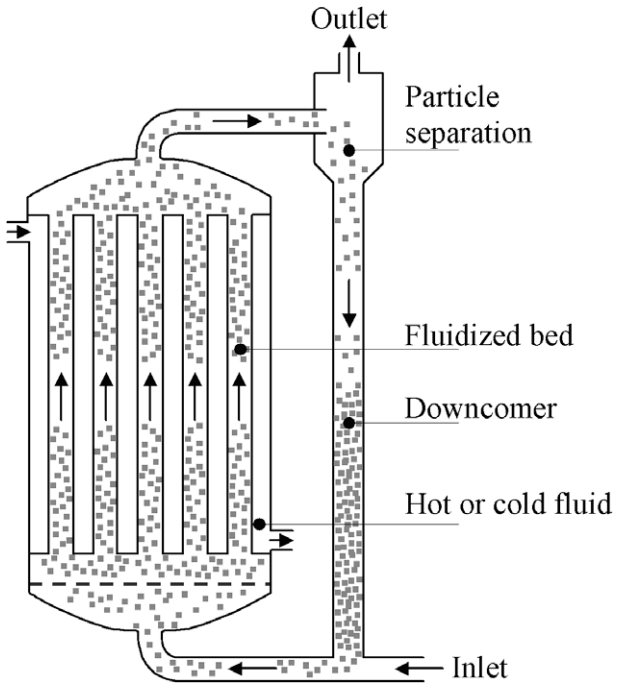

Fig. 1. Schematic layout of a circulating liquid–solid fluidized bed heat exchanger.

30 μs and therefore a sampling frequency of 300 kHz was applied. In order to reduce the amount of measurement data, only collisions with maximum pressures above a certain threshold value were stored for later analysis. The applied threshold values were 0.05, 0.10 and 0.25 bar for 2, 3 and 4 mm particles, respectively.

The piezoelectric sensor was calibrated to determine the elasticity and the effective area of the sensor membrane. For this purpose, the 2, 3 and 4 mm particles were dropped onto the horizontal membrane from heights of 1.0, 5.0 and 20.0 cm corresponding to impact velocities of 0.44, 1.0, and 2.0 m s^{-1}. For the fourth series, a 4 mm particle was bound on a 1-m cord forming a pendulum. The sensor was installed such that the particle hit the vertical membrane in the lowest point of the pendulum. The particles were released from three different horizontal distances from the sensor, namely 1.0, 2.0 and 5.0 cm resulting in impact velocities of 0.031, 0.063 and 0.16 m s^{-1}, respectively. For each particle size and impact velocity, at least 20 impacts were measured. The average values of the maximum pressure and duration of a collision were calculated for each condition.

The duration of a collision between a particle and a surface is, for spherical particles, given by [25]:

$$\tau = 2.5435\left(\frac{1-\upsilon^2}{E}\right)^{0.4}\frac{\rho_p^{0.4} d_p}{v_p^{0.2}} \quad \text{with} \quad E = \frac{E_s E_p}{E_s + E_p} \tag{2}$$

Since the material properties in Eq. (2) are constant for all calibration conditions, the collision duration should be proportional to $d_p v_p^{-0.2}$, which, although the experimental particles differ from spheres, is confirmed in Fig. 3. The combined elasticity E can now be deduced from this proportionality. With a Poisson's ratio of 0.3, the combined elasticity equals 1.06×10^{10} N m^{-2}.

The maximum force of a collision between a particle and a surface is, for spherical particles, given by [25]:

$$F_{max} = 0.7574\left(\frac{E}{1-\upsilon^2}\right)^{0.4}\rho_p^{0.6} d_p^2 v_p^{1.2} \tag{3}$$

This maximum force of a collision is measured by the sensor as a pressure:

$$p_{max} = \frac{F_{max}}{A_s} \tag{4}$$

Despite that the experimental particles are not spherical, Fig. 4 confirms Eqs. (3) and (4) showing a proportionality between the measured maximum pressure and $d_p^2 v_p^{1.2}$. Since the material properties

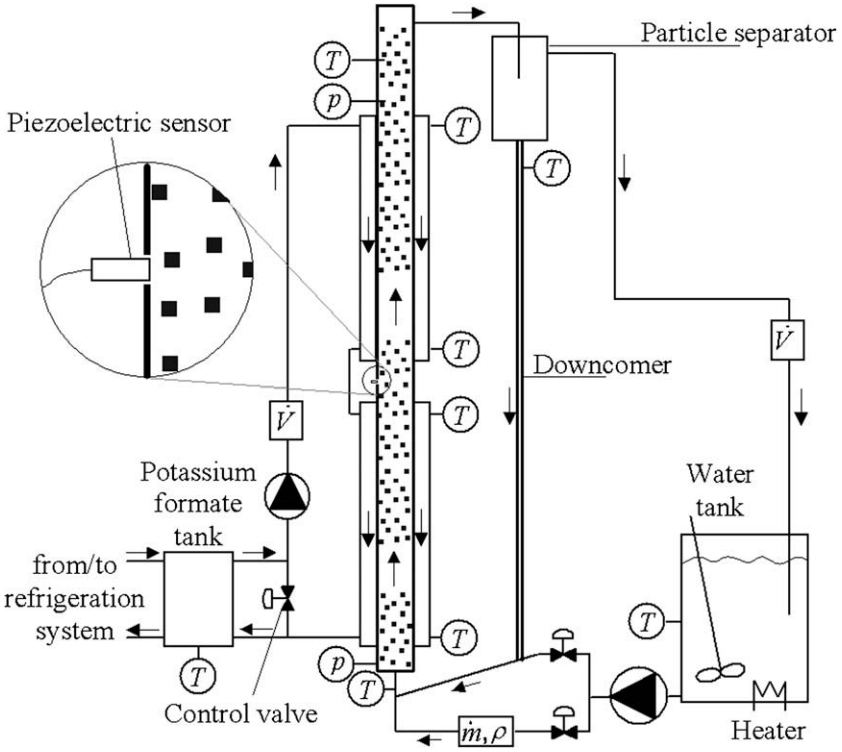

Fig. 2. Schematic layout of experimental set-up.

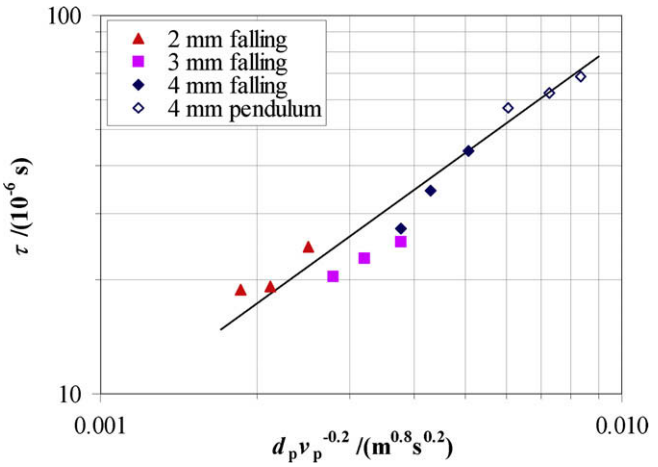

Fig. 3. Contact time as a function of $d_p v_p^{-0.2}$ for 2, 3 and 4 mm particles with various impact velocities.

in Eq. (3) are known, the effective area of the sensor can now be deduced from the relation shown in Fig. 4. The calculated effective area of the sensor is 11.5 mm^2, which corresponds to an effective diameter of 3.8 mm.

2.3. Experimental conditions

First of all, the influences of particle size and bed voidage on the impact characteristics were investigated for stationary fluidized beds as listed in Table 1. The lowest bed voidage for a certain particle size in the table corresponds to the minimum bed voidage for homogenous fluidization. Below this bed voidage, the fluidized bed showed heterogeneous behavior with dilute liquid slugs flowing from bottom to top.

A second series of experiments was carried out with circulating fluidized beds as listed in Table 2. The average upward particle velocity is used as a measure for the circulation rate and is deduced from the slip velocity between liquid and particles:

$$v_z = \frac{u_{s,cfb}}{\varepsilon} - v_{slip}\{\varepsilon, d_p\} \tag{5}$$

The relation between the slip velocity on the one hand and the bed voidage and the particle size on the other hand is derived from the stationary fluidized bed experiments:

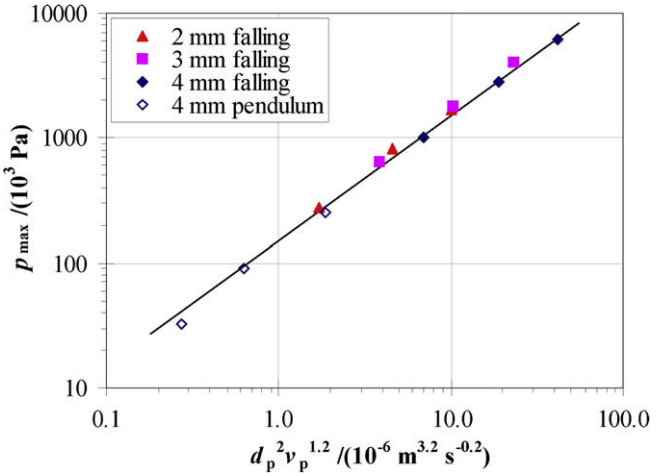

Fig. 4. Measured maximum pressures during collisions as a function of $d_p^2 v_p^{1.2}$ for 2, 3 and 4 mm particles with various impact velocities.

Table 1
Experimental conditions of stationary fluidized bed experiments.

d_p (mm)	ε (%)	u_s (m s^{-1})
2.1	69.4	0.20
	72.7	0.22
	76.2	0.24
	79.4	0.27
	82.7	0.31
	86.2	0.35
	89.7	0.40
	93.2	0.45
	96.2	0.51
3.2	76.0	0.32
	79.0	0.33
	82.5	0.37
	86.0	0.41
	89.5	0.47
	93.0	0.53
	96.0	0.60
4.3	79.8	0.38
	82.6	0.41
	86.6	0.47
	89.7	0.53
	93.4	0.61
	96.3	0.68

$$v_{slip}\{\varepsilon, d_p\} = \frac{u_{s,sfb}\{\varepsilon, d_p\}}{\varepsilon} \tag{6}$$

The control flow through the bottom of the downcomer enabled to control the circulation of particles up to a certain maximum. Most of the experiments were operated at this maximum. For three combinations of particle size and bed voidage, the control flow was varied in order to change the circulation rate while the bed voidage was kept constant.

3. Results

3.1. Analysis of a single experiment

A typical impact measured by the piezoelectric sensor during operation of a stationary fluidized bed of 3 mm particles at a bed voidage of 89.5% is shown in Fig. 5. The contact time of the impact τ is defined as the period that the measured pressure is above the threshold value. The frequency distribution of the contact times

Table 2
Experimental conditions of circulating fluidized bed experiments.

d_p (mm)	ε (%)	u_s (m s^{-1})	v_z (m s^{-1})
2.1	79.0	0.58	0.40
	82.5	0.45	0.17
	82.5	0.54	0.29
	82.5	0.77	0.56
	85.9	1.01	0.77
	88.5	1.24	0.97
	89.5	0.50	0.12
	89.5	0.66	0.29
	89.5	0.88	0.54
3.2	79.0	0.72	0.48
	82.5	0.87	0.61
	85.5	1.05	0.75
	89.5	0.58	0.13
	89.5	0.78	0.34
	89.5	0.97	0.56
	89.5	1.27	0.90
4.3	79.9	0.66	0.36
	83.1	0.82	0.48
	86.4	0.91	0.51
	89.4	1.14	0.69

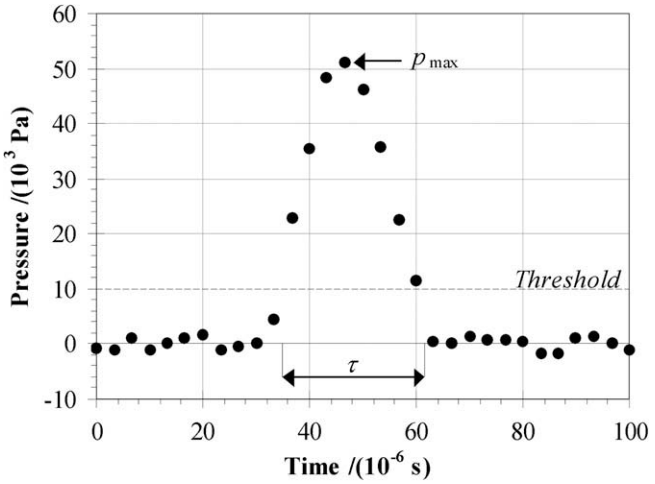

Fig. 5. Measured pressures during a collision of a particle on the sensor.

for the concerned experiment in Fig. 6 is bimodal, which means that two different types of impacts can be distinguished, namely short and long impacts. Similar bimodal distributions were obtained by Zenit et al. [21], who also recorded the particle behavior close to the sensor with a high-speed digital camera. Synchronization of these recordings with the pressure measurements revealed that long impacts are caused by particles that hit the sensor and that the short impacts are caused by liquid pressure fronts induced by collisions between particles in the vicinity of the sensor. Since the time between each data point is 3.3 μs, the shortest impacts extended for only one data point. Fig. 6 indicates that, for these specific experiments, short impacts have contact times less than 13.3 μs.

In the analysis of the experiments, the two types of impacts are considered separately. The particle–wall collisions are characterized by their frequency and their radial impact velocity, which is determined from the measured maximum pressure of each collision and Eqs. (3) and (4). The liquid pressure fronts are characterized by their frequency and maximum pressure.

3.2. Stationary fluidized beds

3.2.1. Particle–wall collisions

An analysis of the particle–wall collisions of a single stationary fluidized bed experiment shows that the distribution of radial impact velocities approaches the Maxwell distribution (see Fig. 7):

$$y_A\{v_r\} = \frac{f_A}{v_{r,avg}\sqrt{\pi}} \exp\left(-\left(\frac{v_r}{2v_{r,avg}}\right)^2\right) \tag{7}$$

This result is in accordance with visual observations by Carlos and Richardson [13], who draw a parallel between the particle motion in fluidized beds and the motion of molecules in gases. The Maxwell distribution was not obtained during the piezoelectric measurements of particle impacts by Meijer et al. [19], since they measured a relatively high number of low-velocity impacts. The probable cause for this deviation is the fact that no distinction was made between the two impact types and that the measured distribution therefore contained both particle–wall collisions and liquid pressure fronts.

For all 22 stationary fluidized bed conditions listed in Table 1, the measured radial particle impact velocity distribution is approached by a Maxwell distribution by fitting the average radial particle velocity $v_{r,avg}$ and the frequency of particle–wall collisions f_A in Eq. (7) (see Fig. 7). The results in Fig. 8 indicate that the average radial impact particle velocity depends barely on the bed voidage and is approximately one-tenth of the superficial liquid velocity:

$$v_{r,avg} = 0.10u_s \tag{8}$$

The fitted frequencies of particle–wall collisions f_A appear to decrease with increasing bed voidage and to be higher for smaller particles. Correlations for this frequency given by [19] can be rewritten into the following form:

$$f_A = v_{r,avg}\frac{6(1-\varepsilon)}{\pi d_p^3} f\{\varepsilon\} \tag{9}$$

Fig. 9 shows that experimentally obtained values for f are indeed only a function of the bed voidage. Correlations for f{ε} can be derived from correlations proposed for the particle pressure, which is the total impulse exerted by particles per square meter wall per second. The particle pressure J of a particle impact velocity distribution as stated in Eq. (7) is given by:

$$J_{p-w} = \int_0^\infty y_A 2m_p v_r dv_r = \frac{2\sqrt{\pi}}{3} f_A d_p^3 \rho_p v_{r,avg} \tag{10}$$

If Eqs. (8) and (10) are applied for the particle pressure correlation proposed by Gidaspow [26], then function f becomes:

$$f\{\varepsilon\} = \frac{\sqrt{\pi}}{3}(1-\varepsilon)g_0 \quad \text{with} \quad g_0 = \left(1-\left(\frac{1-\varepsilon}{1-\varepsilon_{pb}}\right)^{1/3}\right)^{-1} \tag{11}$$

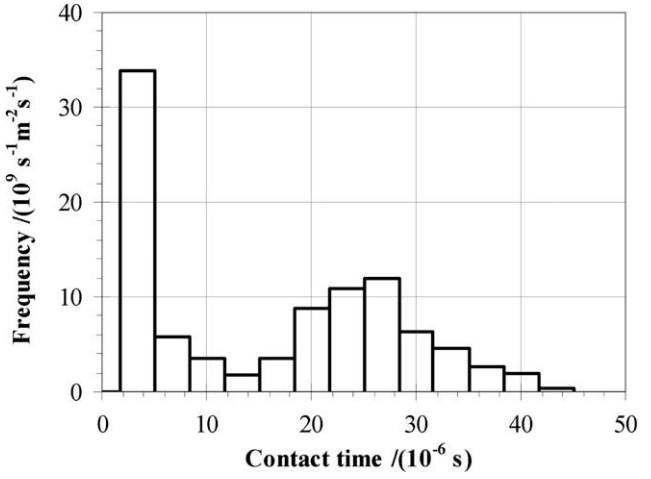

Fig. 6. Frequency distribution of impacts with various contact times (SFB, d_p = 3.2 mm, ε = 89.5%).

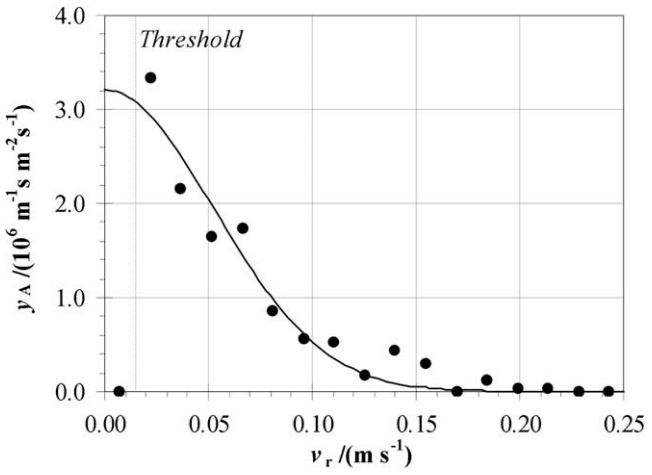

Fig. 7. Frequency distribution of radial particle impact velocities (SFB, d_p = 3.2 mm, ε = 89.5%).

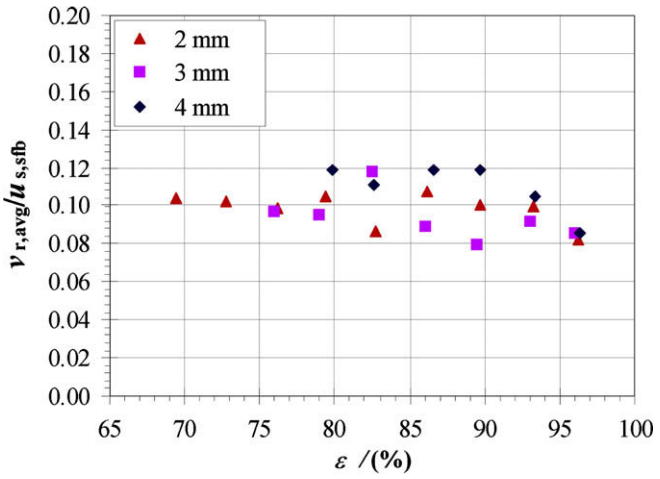

Fig. 8. Ratio between the average radial particle impact velocity and the superficial velocity as function of bed voidage for stationary fluidized beds with different particle sizes.

An adjusted form of Eq. (11) with a packed bed voidage of 40% and a different constant appears to give a good representation of the experimentally obtained values for f as shown in Fig. 9:

$$f\{\varepsilon\} = 2.33(1-\varepsilon)g_{0,adj} \quad \text{with}$$

$$g_{0,adj} = \max\left[3, \left(1-\left(\frac{1-\varepsilon}{1-\varepsilon_{pb}}\right)^{1/3}\right)^{-1}\right] \tag{12}$$

3.2.2. Particle–particle collisions

The measured frequency of liquid pressure fronts induced by particle–particle collisions in stationary fluidized beds is of the same order of magnitude as the number of measured particle–wall collisions. However, measured maximum pressures and contact times are both about a factor of five lower. It is therefore expected that the liquid pressure fronts only give a minor contribution to the total energy and impulse exerted on the wall, which is confirmed in Section 4.2. The influence of liquid pressure fronts on fouling removal in stationary fluidized beds is therefore also expected to be negligible. For this reason, there is no need to model the characteristics of particle–particle collisions in stationary fluidized beds.

3.3. Circulating fluidized beds

3.3.1. Particle–wall collisions

In analogy with the stationary fluidized bed experiments, the average radial particle impact velocities and frequencies were also deduced from the impact measurements of the circulating fluidized bed experiments. The results in Fig. 10 show an increasing trend of the average radial particle impact velocity as the upward particle velocity increases. This trend is similar for the three particle sizes and for various bed voidages. In order to calculate the total energy or impulse exerted on the wall as a function of the circulation rate, this increasing trend is described by the following empirical expression, in which the radial impact velocity for stationary fluidized beds is calculated from Eq. (8):

$$v_{r,avg,cfb} = v_{r,avg,sfb}(1 + 0.68 \cdot v_z) \tag{13}$$

In contrast with the radial impact velocity, the frequency of particle–wall collisions decreases as the upward particle velocity increases as shown in Fig. 11. Since the decrease of collisions occurs especially at low upward particle velocities, the frequency is described by an empirical exponential expression, in which the frequency for stationary fluidized beds is calculated from Eqs. (9) and (12):

$$f_{A,cfb} = f_{A,sfb} \cdot \exp(-1.09 \cdot v_z) \tag{14}$$

The measured differences between particle–wall collisions in stationary and circulating fluidized beds are attributed to changes in the motion and distribution of particles. During homogeneous fluidization in stationary fluidized beds, particles are uniformly distributed in both axial and radial direction [27]. For circulating fluidized beds however, several researchers have reported non-uniform particle distributions. Experiments by Liang et al. [28,29] for example, showed that the concentration of 0.4 mm glass spheres in a circulating fluidized bed of 140 mm in diameter is higher near the wall than in the core of the bed. These experimental results were confirmed by CFD simulations presented by Cheng and Zhu [30]. In addition, they showed that the non-uniformity increases as the ratio between the bed and particle diameter increases. Opposite experimental results were obtained by Kim and Lee [31], who observed that 3 mm glass spheres move to the center of a 12 mm tube as the upward particle velocity is increased. Moreover, it was observed that the frequency of particle–wall collisions decreases with increasing upward particle velocity, which is in accordance with the experimental results obtained in this work. A lower collision

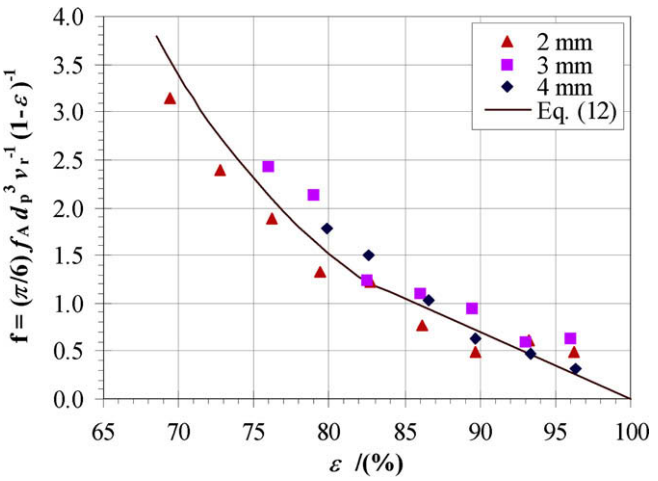

Fig. 9. Function f{ε} for stationary fluidized beds with different particle sizes.

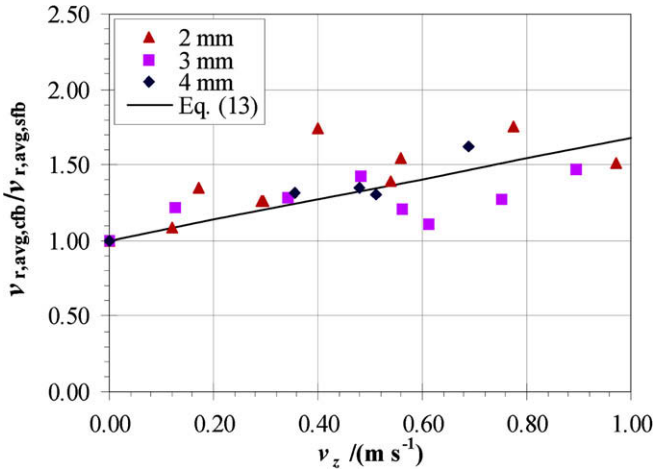

Fig. 10. Relative average radial particle impact velocity in circulating fluidized beds.

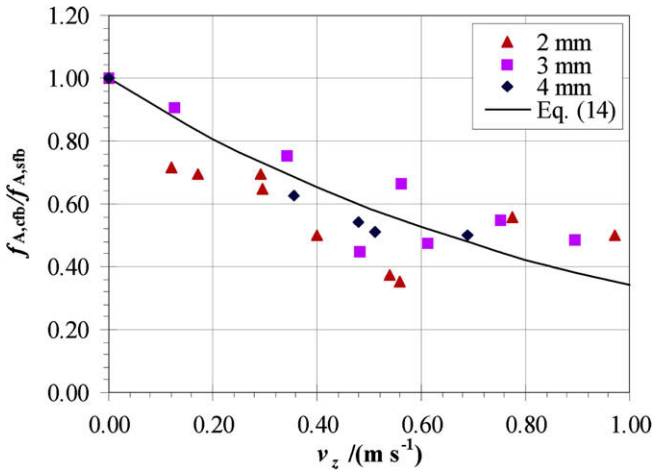

Fig. 11. Relative frequency of particle–wall collisions in circulating fluidized beds.

frequency at higher circulation rates was also reported by Garić-Grulović et al. [16] for 5 mm glass spheres in a rectangular fluidized bed of 60 × 8 mm. At low circulation rates the particles move vertically with some radial movement, but at higher circulation rates the particles follow vertical streamlines resulting in less particle–wall collisions.

3.3.2. Particle–particle collisions

The frequency and average maximum pressure of liquid pressure fronts measured during circulation were both considerably higher than during stationary operation. It is therefore considered as a possibility that the liquid pressure fronts induced by particle–particle collisions do play a role in the removal of fouling. For this reason, the distribution of liquid pressure fronts that reach the wall are analyzed for the circulating fluidized bed experiments.

As discussed in Section 3.1, the short impacts measured by the piezoelectric sensor are assumed to be caused by liquid pressure fronts induced by particle–particle collisions in the vicinity of the sensor. In order to characterize the liquid pressure fronts, the particle–particle collisions are therefore characterized first. According to Carlos and Richardson [13], particle velocities in a fluidized bed are distributed like a Maxwell distribution and it is therefore assumed that particle–particle collision velocities can also be described with this distribution:

$$y_V\{v_p\} = \frac{f_V}{v_{p,avg}\sqrt{\pi}} \exp\left(-\left(\frac{v_p}{2v_{p,avg}}\right)^2\right) \tag{15}$$

According to collision mechanics, the maximum force during a collision between two spherical particles is proportional to the collision velocity to the power 1.2 [25]. It is therefore assumed that the maximum pressure of a pressure front generated by a particle–particle collision is also proportional to the collision velocity to the power 1.2. The distribution of maximum pressures at a distance d_p from the point of collision is therefore:

$$y_V\{p_{max}\} = \frac{f_V}{2\Gamma\{8/5\}p_{max,avg}} \exp\left(-\left(\frac{p_{max}}{2p_{max,avg}}\right)^{5/3}\right) = 0.5596\frac{f_V}{p_{max,avg}} \exp\left(-\left(\frac{p_{max}}{2p_{max,avg}}\right)^{5/3}\right) \tag{16}$$

The distribution of pressure fronts reaching a point at the wall is obtained by integration of all pressure fronts coming from particle–particle collisions in an infinite hemispherical volume V. Since the maximum pressure of a front decreases approximately quadratically with the distance r [20,32], the distribution of maximum pressures at the wall is:

$$y_j\{p_{max}\} = 0.5596\frac{f_V}{p_{max,avg}} \int_V \exp\left(-\left(\frac{p_{max}(r/d_p)^2}{2p_{max,avg}}\right)^{5/3}\right) dV \tag{17}$$

The integration over volume V is performed in polar coordinates, where the integral over distance r is taken from $d_p/2$ to infinity, since the point of collision cannot be closer to the wall than a half particle diameter:

$$y_j\{p_{max}\} = 0.5596\frac{f_V d_p^2}{p_{max,avg}} \int_0^{\pi}\int_0^{\pi}\int_{d_p/2}^{\infty} \times \exp\left(-\left(\frac{p_{max}(r/d_p)^2}{2p_{max,avg}}\right)^{5/3}\right)\left(\frac{r}{d_p}\right)^2 \sin\varphi dr d\varphi d\theta \tag{18}$$

Integration for φ and θ and substitution of r/d_p by l leads to:

$$y_j\{p_{max}\} = 3.516\frac{f_V d_p^3}{p_{max,avg}} \int_{1/2}^{\infty} l^2 \times \exp\left(-\left(\frac{p_{max}}{2p_{max,avg}}\right)^{5/3} l^{10/3}\right) dl \quad \text{with} \quad l = \frac{r}{d_p} \tag{19}$$

The integral in Eq. (19) cannot be solved analytically and is therefore approximated by a numerical solution:

$$y_j\{p_{max}\} \approx b p_{max}^{-3/2} \exp\left(-\left(\frac{p_{max}}{a}\right)^{1.6}\right) \quad \text{with}$$
$$a = 9.548 p_{max,avg} \quad \text{and} \quad b = 3.188 f_V d_p^3 p_{max,avg}^{1/2} \tag{20}$$

The maximum pressures of pressure fronts measured during the circulating fluidized bed experiments were used to fit parameters a and b in Eq. (20) with a least square method for $y_j p_{max}^{3/2}$. The result of this method for a fluidized bed of 3 mm particles, a bed voidage of 89.5% and an upward particle velocity of 0.90 m s^{-1} is compared with the measured distribution in Fig. 12. The figure demonstrates that the distribution given by Eq. (20) corresponds well with the experimental distribution.

The average maximum pressure at a distance d_p from a particle–particle collision $p_{max,avg}$ and the frequency of particle–particle collisions f_V are deduced from parameters a and b for each experimental condition by Eq. (20). The obtained average maximum pressures increase approximately linearly with the net upward particle velocity, which is explained by heavier particle–particle collisions at higher circulation rates. From this is expected that the collision velocity is mainly determined by the upward particle velocity. However, particle–particle collisions also occur during stationary fluidization when the net upward particle velocity is zero. The assumption is therefore made that the average collision velocity can be approached by the superposition of the net upward particle velocity and the average particle velocity during stationary fluidization:

$$v_{p,avg} = v_z + v_{p,avg,sfb} \tag{21}$$

According to Carlos and Richardson [13], the average particle velocity in stationary fluidized beds is approximately three times the average radial particle velocity, which can be determined from Eq. (8). The average particle–particle collision velocity in circulating fluidized beds is therefore modeled as:

$$v_{p,avg} = v_z + 3v_{r,avg,sfb} \tag{22}$$

The assumption that the average maximum pressure of a pressure front induced by a particle–particle collision is proportional to the velocity of this collision is confirmed by Fig. 13. From this figure,

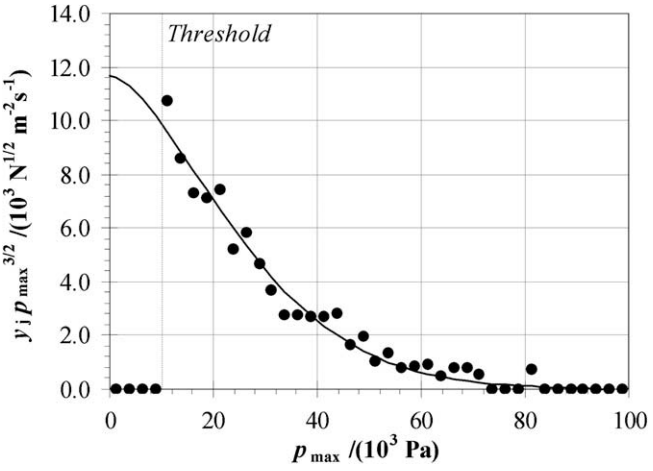

Fig. 12. Distribution $y_j {p_{max}}^{3/2}$ of liquid pressure fronts (CFB, d_p = 3.2 mm, ε = 89.5%, v_z = 0.90 m s^{-1}).

the following correlation is deduced for the average maximum pressure at a distance d_p from a particle–particle collision:

$$p_{max,avg} = 3.430 \times 10^3 v_{p,avg}^{6/5} \tag{23}$$

Besides the average pressure, the particle–particle collision frequency f_V also shows an increasing trend as the net upward particle velocity increases. According to Gidaspow [26], the theoretical number of particle–particle collisions in a fluidized bed of spheres per unit of volume per unit time is:

$$f_V = \frac{144}{\pi\sqrt{3\pi}} \frac{g_0(1-\varepsilon)^2 v_{p,avg}}{d_p^4} \tag{24}$$

In order to show the isolated effect of the particle velocity as defined in Eq. (21), the fitted frequencies f_V are multiplied by $d_p^4 g_{0,adj}{}^{-1}(1-\varepsilon)^{-2}$ in Fig. 14. The figure indicates that the correlation in Eq. (24) describes the measured trends well, but with a different constant. The following correlation is deduced from the figure:

$$f_V = 5.405 \frac{g_{0,adj}(1-\varepsilon)^2 v_{p,avg}}{d_p^4} \tag{25}$$

4. Discussion

In the previous section, models to characterize the impacts on the wall of a liquid–solid fluidized bed were obtained from experiments. In this section, these models are used to investigate how the impulse exerted on the wall and the energy of impacts depend on fluidized bed parameters such as particle size, bed voidage and circulation rate.

4.1. Stationary fluidized beds

Since the contribution of liquid pressure fronts to the total impulse and the total energy are negligible for stationary fluidized beds as stated in Section 3.2, only contributions of particle–wall collisions are taken into account in the analysis.

4.1.1. Impulse exerted on the wall

The total impulse exerted by particles hitting the wall is given by:

$$J_{p-w} = \int_0^\infty y_A j_{p-w} dv_r \tag{26}$$

The distribution of impact velocities in Eq. (7) is substituted in Eq. (26). In addition, particle–wall collisions are considered as fully elastic with an impulse of $2m_p v_r$ per impact:

$$J_{p-w} = \int_0^\infty \frac{f_A}{v_{r,avg}\sqrt{\pi}} \exp\left(-\left(\frac{v_r}{2v_{r,avg}}\right)^2\right) 2m_p v_r dv_r = \frac{2\sqrt{\pi}}{3} f_A d_p^3 \rho_p v_{r,avg} \tag{27}$$

Substitution of Eqs. (9) and (12) for the particle–wall frequency f_A in Eq. (27) gives an expression for the total impulse:

$$J_{p-w} = 5.26 g_{0,adj}(1-\varepsilon)^2 v_{r,avg}^2 \rho_p \tag{28}$$

The equivalent particle diameter d_p is not explicitly present in Eq. (28). The cause for this absence is the fact that the higher impulse per collision for larger particles is exactly compensated by the lower number of collisions.

Combining Eqs. (8) and (28) and the application of a particle material density of 7900 kg m^{-3} gives a final expression for the total impulse exerted by particles on the wall:

$$J_{p-w} = 4.15 \times 10^2 g_{0,adj}(1-\varepsilon)^2 u_{s,sfb}^2 \tag{29}$$

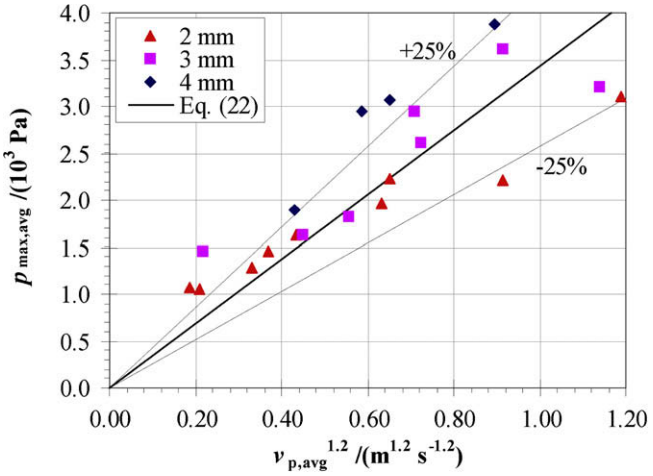

Fig. 13. Measured average pressures of pressure fronts as function of particle velocity to the power 1.2.

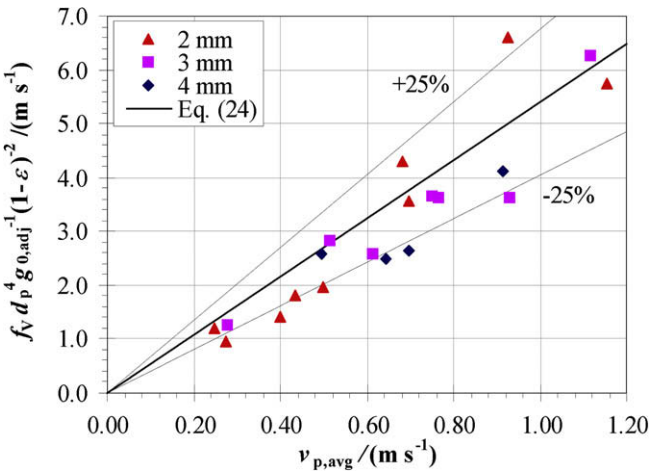

Fig. 14. Normalized frequency of particle–particle collisions as function of particle velocity.

The results of Eq. (29) for the studied conditions in Fig. 15 show that the impulse on the wall increases monotonously with a decreasing bed voidage. The higher impulse for bigger particle sizes is solely caused by the higher particle velocity induced by a higher superficial velocity.

4.1.2. Energy of impacts

The total energy of impacts in stationary fluidized beds is calculated from the kinetic energy of all particles that hit the wall:

$$E_{p-w} = \int_0^\infty y_A e_{p-w} dv_r \tag{30}$$

The distribution of particle–wall collision velocities in Eq. (7) is substituted in Eq. (30) and the kinetic energy per particle is given by $\frac{1}{2}m_p v_r^2$:

$$E_{p-w} = \int_0^\infty \frac{f_A}{v_{r,avg}\sqrt{\pi}} \exp\left(-\left(\frac{v_r}{2v_{r,avg}}\right)^2\right)\frac{1}{2}m_p v_r^2 dv_r = \frac{\pi}{6} f_A d_p^3 \rho_p v_{r,avg}^2 \tag{31}$$

Substitution of Eqs. (9) and (12) for the particle–wall frequency f_A gives an expression for the total energy:

$$E_{p-w} = 2.33 g_{0,adj}(1-\varepsilon)^2 \rho_p v_{r,avg}^3 \tag{32}$$

Finally, the relation between the particle and superficial velocity from Eq. (8) and the particle density of 7900 kg m^{-3} are substituted in Eq. (32). The result is an expression for the total kinetic energy of all particles hitting the wall:

$$E_{p-w} = 18.4 g_{0,adj}(1-\varepsilon)^2 u_{s,sfb}^3 \tag{33}$$

A graphical representation of Eq. (33) in Fig. 16 shows roughly the same behavior for the total energy as for the total impulse in Fig. 15. The total kinetic energy of particles hitting the wall also increases with decreasing bed voidage and is higher for bigger particles. However, the relative differences between different particle sizes is larger in Fig. 16, which is caused by the stronger influence of the superficial velocity.

4.2. Circulating fluidized beds

In contrast with the analysis for stationary fluidized beds, both contributions from particle–wall collisions and liquid pressure fronts need to be taken into account in the analysis of circulating fluidized beds.

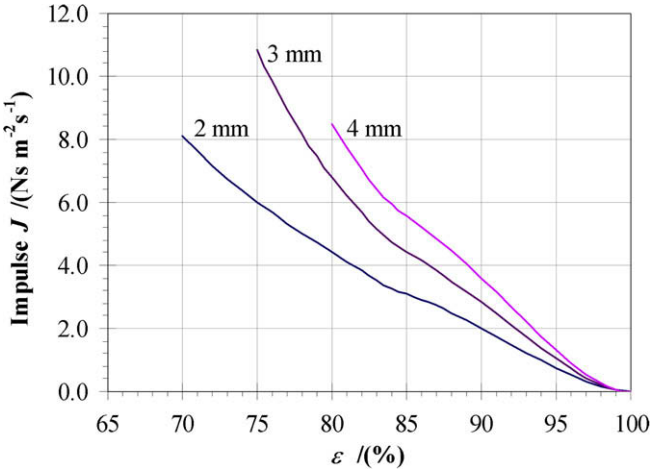

Fig. 15. Impulse exerted by impacts on the wall of a stationary fluidized bed.

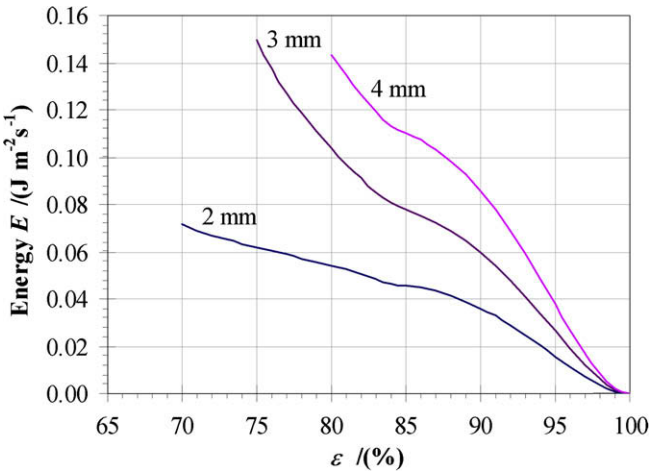

Fig. 16. Energy of impacts on the wall of a stationary fluidized bed.

4.2.1. Impulse exerted on the wall

The total impulse exerted on the wall is given by the sum of the impulse by particle–wall collisions and by liquid pressure fronts:

$$J_{cfb} = J_{p-w} + J_{lpf} \tag{34}$$

The impulse by particle–wall collisions in circulating fluidized beds is obtained by substitution of Eqs. (13) and (14) in Eq. (27):

$$J_{p-w} = \frac{2\sqrt{\pi}}{3} f_{A,sfb} d_p^3 \rho_p v_{r,avg,sfb}(1 + 0.68 \cdot v_z)\exp(-1.09 \cdot v_z) \tag{35}$$

Analogously with the method described in Section 4.1 for stationary operation, the final expression for the impulse of particle–wall collisions is obtained by substitution of Eqs. (8), (9), and (12) in Eq. (35):

$$J_{p-w} = 4.15 \times 10^2 g_{0,adj}(1-\varepsilon)^2 u_{s,sfb}^2 (1 + 0.68 \cdot v_z)\exp(-1.09 \cdot v_z) \tag{36}$$

The total impulse exerted by liquid pressure fronts is given by the sum of the impulses of all individual pressure fronts:

$$J_{lpf} = \int_0^\infty y_j j_{lpf} dp_{max} \tag{37}$$

The impulse exerted by a single liquid pressure front per m^2 is given by:

$$j_{lpf} = \int_0^\tau p dt = \frac{2}{\pi} p_{max} \tau_{lpf} \tag{38}$$

Replacement of the impact of a single pressure front and the distribution of pressure fronts in Eq. (37) by Eqs. (38) and (20), respectively, leads to:

$$J_{lpf} = \frac{2}{\pi}\int_0^\infty b p_{max}^{-3/2} \exp\left(-\left(\frac{p_{max}}{a}\right)^{1.6}\right) p_{max} \tau_{lpf} dp_{max} \tag{39}$$

The duration of a particle–particle collision is given by Goldsmith [25]. The application of the material properties for stainless steel results in an expression for the duration of a collision as a function of the particle size and the collision velocity:

$$\tau_{p-p} = 2.922 \rho_p^{0.4}\left(\frac{1-\upsilon^2}{E_p}\right)^{0.4} d_p v_p^{-1/5} = 3.016 \cdot 10^{-3} d_p v_p^{-1/5} \tag{40}$$

The relation between the particle collision velocity and the maximum pressure of the resulting pressure front from Eq. (23) is combined with Eq. (40):

$$\tau_{p-p} = 1.171 \times 10^{-2} d_p p_{max}^{-1/6} \tag{41}$$

The calculated results from Eq. (41) for the duration of particle–particle collisions correspond fairly to the measured durations of pressure fronts. It is therefore assumed that both durations are equal:

$$\tau_{lpf} = \tau_{p-p} \tag{42}$$

Substitution of Eqs. (41) and (42) in Eq. (39) gives:

$$J_{lpf} = 7.456 \cdot 10^{-3} d_p b \int_0^{\infty} p_{max}^{-2/3} \exp\left(-\left(\frac{p_{max}}{a}\right)^{1.6}\right) dp_{max} \tag{43}$$

In Eq. (43), the ratio p_{max}/a is replaced by x:

$$J_{lpf} = 7.456 \times 10^{-3} d_p b a^{1/3} \int_0^{\infty} x^{-2/3} \exp(-x^{1.6}) dx \quad \text{with} \quad x = \frac{p_{max}}{a} \tag{44}$$

The integral in Eq. (44) is solved numerically and parameters a and b are replaced by the correlation in Eq. (20):

$$J_{lpf} = 0.1386 f_V d_p^4 p_{max,avg}^{5/6} \tag{45}$$

Combination of Eqs. (23), (25), and (45) leads to a final expression for the impulse exerted by pressure fronts on the wall:

$$J_{lpf} = 6.62 \times 10^2 g_{0,adj} (1-\varepsilon)^2 v_{p,avg}^2 \tag{46}$$

As stated in Eq. (34), the total impulse on the wall is the sum of the impulse exerted by particle–wall collisions (Eq. (36)) and the impulse exerted by pressure fronts (Eq. (46)). Fig. 17 gives a graphical representation of both contributions as a function of the upward particle velocity for a fluidized bed of 3 mm particles at a bed voidage of 89.5%. The figure shows a slight decrease of impulse exerted by particle–wall collisions as the upward particle velocity increases. This decrease is caused by a reduced number of collisions during circulation, which is only partly compensated by the higher impact velocity. The contribution of pressure fronts strongly increases as the upward particle velocity increases and exceeds the contribution of particle–wall collisions at upward particle velocities higher than 0.22 m s^{-1} for this example. At stationary circulation ($v_z = 0$) however, the impulse of pressure fronts is calculated to be only about 10% of the total impulse for all conditions.

4.2.2. Energy of impacts

The total energy of impacts on the wall is the sum of the energy of the particles hitting the wall and the energy of liquid pressure fronts:

$$E_{cfb} = E_{p-w} + E_{lpf} \tag{47}$$

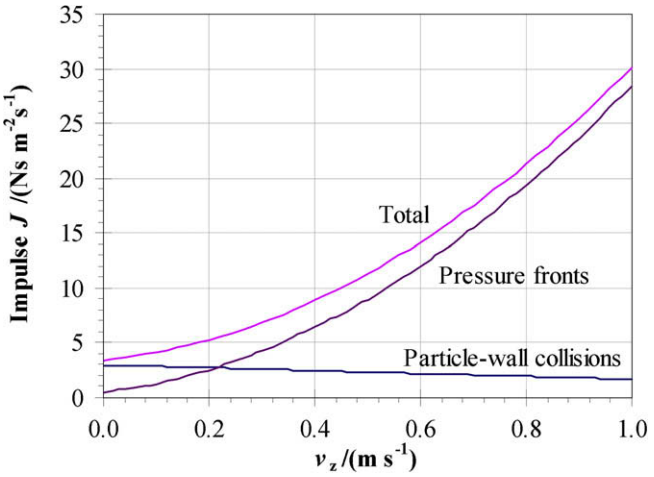

Fig. 17. Impulse exerted by impacts on the wall of a circulating fluidized bed of 3 mm particles at a bed voidage of 89.5%.

The total kinetic energy of particles hitting the wall in a circulating fluidized bed is obtained by substitution of Eqs. (13) and (14) in Eq. (31):

$$E_{p-w} = \frac{\pi}{6} f_{A,sfb} d_p^3 \rho_p v_{r,avg,sfb}^2 (1 + 0.68 \cdot v_z)^2 \exp(-1.09 \cdot v_z) \tag{48}$$

Analogously with the method described in Section 4.1 for stationary operation, the final expression for the energy of particles is obtained by substitution of Eqs. (8), (9), and (12) in Eq. (48):

$$E_{p-w} = 18.4 g_{0,adj} (1-\varepsilon)^2 u_{s,sfb}^3 (1 + 0.68 \cdot v_z)^2 \exp(-1.09 \cdot v_z) \tag{49}$$

The total energy of pressure fronts is the sum of the energy per m^2 of all pressure fronts reaching a point at the wall:

$$E_{lpf} = \int_0^{\infty} y_j e_{lpf} dp_{max} \tag{50}$$

The energy of a single liquid pressure front per m^2 is [33]:

$$e_{lpf} = \int_0^{\tau} \frac{p^2}{\rho_{liq} c_{liq}} dt = \frac{p_{max}^2 \tau_{lpf}}{2 \rho_{liq} c_{liq}} \quad \text{with} \quad p\{t\} = p_{max} \sin\left(\frac{\pi t}{\tau_{lpf}}\right) \tag{51}$$

Replacement of the energy per pressure front and the distribution of pressure fronts in Eq. (50) by Eqs. (51) and (20), respectively, leads to:

$$E_{lpf} = \frac{b}{2 \rho_{liq} c_{liq}} \int_0^{\infty} p_{max}^{1/2} \exp\left(-\left(\frac{p_{max}}{a}\right)^{1.6}\right) \tau dp_{max} \tag{52}$$

The expression for the duration of a pressure front in Eqs. (41) and (42) is applied in Eq. (52):

$$E_{lpf} = 5.86 \times 10^{-3} \frac{d_p b}{\rho_{liq} c_{liq}} \int_0^{\infty} p_{max}^{1/3} \exp\left(-\left(\frac{p_{max}}{a}\right)^{1.6}\right) dp_{max} \tag{53}$$

In Eq. (53), the ratio p_{max}/a is replaced by x:

$$E_{lpf} = 5.86 \times 10^{-3} \frac{a^{4/3} b d_p}{\rho_{liq} c_{liq}} \int_0^{\infty} x^{1/3} \exp(-x^{1.6}) dx \quad \text{with} \quad x = \frac{p_{max}}{a} \tag{54}$$

The integral for x in Eq. (54) is solved numerically. The parameters a and b are replaced by the correlations given in Eq. (20):

$$E_{lpf} = 0.3061 \frac{f_V d_p^4 p_{max,avg}^{11/6}}{\rho_{liq} c_{liq}} \tag{55}$$

The correlation in Eq. (23) is now used to replace the average maximum pressure by the average particle velocity:

$$E_{lpf} = 9.273 \times 10^5 \frac{f_V d_p^4 v_{p,avg}^{11/5}}{\rho_{liq} c_{liq}} \tag{56}$$

Finally, the correlation for the frequency of particle–particle collisions in Eq. (25) and the values for density (998 kg m^{-3}) and speed of sound (1482 m s^{-1}) are substituted in Eq. (56) resulting in a final expression for the energy of pressure fronts reaching the wall:

$$E_{lpf} = 3.388 g_{0,adj} (1-\varepsilon)^2 v_{p,avg}^{16/5} \tag{57}$$

Both the kinetic energy of particles hitting the wall (Eq. (49)) and the energy of liquid pressure fronts (Eq. (57)) are shown in Fig. 18 for a fluidized bed of 3 mm particles at a bed voidage of 89.5%. The kinetic energy of the particles is almost constant in the figure, because the lower collision frequency is compensated by the strong increase of the kinetic energy per collision (Eq. (49)). The energy of liquid pressure fronts is only 0.6% of the total energy for stationary fluidized beds, but increases considerably as the upward particle velocity increases.

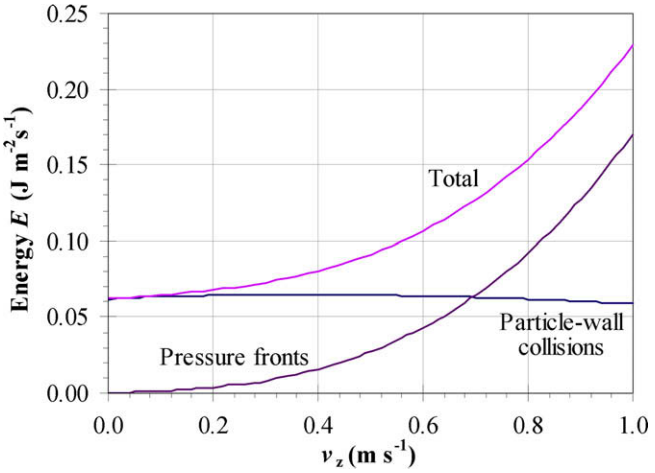

Fig. 18. Energy of impacts on the wall of a circulating fluidized bed of 3 mm particles at a bed voidage of 89.5%.

4.3. Expectations for fouling removal

As already mentioned in the introduction, it is not clear up to now how particle–wall collisions are related to fouling removal. In literature, the removal of deposits is supposed to be proportional to the energy of particles hitting the wall [18,24] or to the total impulse exerted by particles on the wall [23]. Based on these ideas, expectations for the fouling removal ability of various fluidized beds can be made with the help of the expressions for impulse and energy deduced in this paper. In [34], these expectations are compared to fouling prevention data for a fluidized bed heat exchanger for ice crystal production.

4.3.1. Stationary fluidized beds

Since both the impulse on the wall in Fig. 15 and the kinetic energy of particles in Fig. 16 are higher for large particles, it is expected that fluidized beds consisting of large particles result in better fouling removal. This expectation is in correspondence with experimental results by Meijer [18,24], who showed that the prevention of calcium sulphate fouling by 2 mm particles was better than by 1 mm particles. Experiments with different bed voidages are lacking, but from Figs. 15 and 16 is expected that the fouling removal ability enhances as the bed voidage decreases. The maximum kinetic energy of particles and the maximum impulse are both obtained at the lowest possible bed voidage with homogeneous fluidization. At lower bed voidage, heterogeneous fluidization occurs, which is believed to have a lower fouling removal ability than the homogeneous regime.

Although the particle material density was not varied in the experiments presented in this paper, it is expected to be an important factor in fouling removal. According to Eqs. (28) and (32), the impulse and energy are both proportional to the particle density. Furthermore, it is believed that the radial particle impact velocity is higher for denser particles since a higher superficial velocity is necessary for fluidization. This positive influence of the particle density is confirmed by Rautenbach et al. [6], who showed that calcium sulphate fouling was prevented up to higher heat fluxes by stainless steel particles with a density of 7900 kg m^{-3} than by aluminum oxide particles of 3780 kg m^{-3}. Another factor that might influence fouling removal is the shape of the particles. However, this influence cannot be deduced from the analysis in this paper and experimental results on this topic are lacking.

4.3.2. Circulating fluidized beds

The main difference in impact characteristics between stationary and circulating fluidized beds is the contribution of liquid pressure fronts to the total impulse and the total energy as shown in Figs. 17 and 18. Due to this contribution, both the impulse exerted on the wall and the kinetic energy of impacts strongly increase as the circulation rate increases. It is likely that the liquid pressure fronts contribute to the removal of fouling, since it was shown by several researchers that fouling can be removed by acoustic waves [35–37]. However, it is questionable whether the fouling removal ability of liquid pressure fronts is of the same order of magnitude as the removal ability of particle–wall collisions.

If liquid pressure fronts indeed play a role in fouling removal, it is expected that circulating fluidized beds have a higher fouling removal ability than stationary fluidized beds. Experiments with calcium sulphate fouling by Rautenbach et al. [6] seem to support this statement. Although not all operating conditions are clearly stated, it is obvious from their results that the maximum heat flux at which fouling is prevented, is considerably higher in circulating fluidized beds than in stationary fluidized beds.

5. Conclusions

Heat exchanger fouling in liquid–solid fluidized beds is prevented by two types of impacts on the wall. The first type of impacts is caused by particles hitting the wall, while the second type is caused by liquid pressure fronts induced by particle–particle collisions in the vicinity of the wall. The fouling removal ability of a fluidized bed is believed to be determined by the total impulse exerted on the wall or the total kinetic energy of impacts. In stationary fluidized beds, both parameters are mainly determined by particle–wall collisions, and increase as the particle size increases or as the bed voidage decreases. In circulating fluidized beds, the contribution of liquid pressure fronts to the total impulse and total energy strongly increases as the circulation rate increases. Due to this increase, the fouling removal ability of circulating fluidized beds is expected to be higher than of stationary fluidized beds.

References

[1] T.R. Bott, Fouling of Heat Exchangers, Elsevier, Amsterdam, 1995.
[2] B.A. Garrett-Price, S.A. Smith, R.L. Watts, J.G. Knudsen, W.J. Marner, J.W. Suitor, Fouling of Heat Exchangers. Characteristics: Costs, Prevention, Control, and Removal, Noyes, Park Ridge, 1985.
[3] N.S. Tavare, Industrial Crystallization: Process Simulation Analysis and Design, Plenum, New York, 1995.
[4] H. Müller-Steinhagen, Handbook Heat Exchanger Fouling: Mitigation and Cleaning Technologies, Rugby Institution of Chemical Engineers, 2000.
[5] D.G. Klaren, Self cleaning heat exchangers, in: H. Müller-Steinhagen (Ed.), Handbook Heat Exchanger Fouling: Mitigation and Cleaning Technologies, Rugby Institution of Chemical Engineers, 2000, pp. 186–199.
[6] R. Rautenbach, C. Erdmann, J.S. Kolbach, The fluidized bed technique in the evaporation of wastewaters with severe fouling/scaling potential – latest developments, applications, limitations, Desalination 81 (1991) 285–298.
[7] M. Haid, H. Martin, H. Müller-Steinhagen, Heat transfer to liquid–solid fluidized beds, Chem. Eng. Process. 33 (1994) 211–225.
[8] M. Haid, Correlations for the prediction of heat transfer to liquid–solid fluidized beds, Chem. Eng. Process. 36 (1997) 143–147.
[9] M. Aghajani, H. Müller-Steinhagen, M. Jamialahmadi, New design equations for liquid/solid fluidized bed heat exchangers, Int. J. Heat Mass Transfer 48 (2005) 317–329.
[10] R. Rautenbach, T. Katz, Survey of long time behavior and costs of industrial fluidized bed heat exchangers, Desalination 108 (1996) 335–344.
[11] J.W. Meewisse, C.A. Infante Ferreira, Validation of the use of heat transfer models in liquid/solid fluidized beds for ice slurry generation, Int. J. Heat Mass Transfer 46 (2003) 3683–3695.
[12] P. Pronk, J.W. Meewisse, C.A. Infante Ferreira, Erratum to "Validation of the use of heat transfer models in liquid/solid fluidized beds for ice slurry generation" [Int. J. Heat Mass Transfer 46 (2003) 3683–3695], Int. J. Heat Mass Transfer 48 (2005) 3478–3483.

[13] C.R. Carlos, J.F. Richardson, Solids movement in liquid fluidised beds – I. Particle velocity distribution, Chem. Eng. Sci. 23 (1968) 813–824.
[14] A. Kmieć, Particle distributions and dynamics of particle movement in solid–liquid fluidized beds, Chem. Eng. J. 15 (1978) 1–12.
[15] Ž.B. Grbavčić, D.V. Vuković, F.K. Zdanski, Tracer particle movement in a two-dimensional water-fluidized bed, Powder Technol. 62 (1990) 199–201.
[16] R.V. Garić-Grulović, Ž.B. Grbavčić, Z.L. Arsenijević, Heat transfer and flow pattern in vertical liquid–solids flow, Powder Technol. 145 (2004) 163–171.
[17] J. Bordet, O. Borlai, F. Vergnes, P. Le Goff, Direct measurement of the kinetic energy of particles and their frequency of collision against a wall in a liquid–solids fluidized bed, Inst. Chem. Eng. Symp. Ser. 30 (1968) 165–173.
[18] J.A.M. Meijer, Inhibition of calcium sulphate scale by a fluidized bed, Ph.D. Thesis, Delft University of Technology (The Netherlands), 1984.
[19] J.A.M. Meijer, J.A. Wesselingh, A. Clobus, M.L.A. Goossens, Impacts against the wall of a scaled-up fluidized bed, Desalination 58 (1986) 1–18.
[20] R. Zenit, Collisional mechanics in solid–liquid flows, Ph.D. Thesis, California Institute of Technology (USA), 1997.
[21] R. Zenit, M.L. Hunt, C.E. Brennen, Collisional particle pressure measurements in solid–liquid flows, J. Fluid Mech. 353 (1997) 261–283.
[22] R. Zenit, M.L. Hunt, C.E. Brennen, On the direct and radiated components of the collisional particle pressure in liquid–solid flows, Appl. Sci. Res. 58 (1998) 305–317.
[23] P. Buffière, R. Moletta, Collision frequency and collisional particle pressure in three-phase fluidized beds, Chem. Eng. Sci. 55 (2000) 5555–5563.
[24] J.A.M. Meijer, Prevention of calcium sulphate scale deposition by a fluidized bed, Desalination 47 (1983) 3–15.
[25] W. Goldsmith, Impact: The Theory and Physical Behaviour of Colliding Solids, Arnold, London, 1960. pp. 82–144.
[26] D. Gidaspow, Multiphase Flow and Fluidization: Continuum and Kinetic Theory Descriptions, Academic Press, Boston, 1994. pp. 239–296.
[27] M. Kwauk, Fluidization: Idealized and Bubbleless, with Applications, Science Press, Beijing, 1992.
[28] W.-G. Liang, J.-X. Zhu, Y. Jin, Z.-Q. Yu, Z.-W. Wang, J. Zhou, Radial nonuniformity of flow structure in a liquid–solid circulating fluidized bed, Chem. Eng. Sci. 51 (1996) 2001–2010.
[29] W.-G. Liang, S. Zhang, J.-X. Zhu, Y. Jin, Z.-Q. Yu, Z.-W. Wang, Flow characteristics of the liquid–solid circulating fluidized bed, Powder Technol. 90 (1997) 95–102.
[30] Y. Cheng, J. Zhu, CFD modelling and simulation of hydrodynamics in liquid–solid circulating fluidized beds, Can. J. Chem. Eng. 83 (2005) 177–185.
[31] N.H. Kim, Y.P. Lee, Hydrodynamic and heat transfer characteristics of glass bead-water flow in a vertical tube, Desalination 133 (2001) 233–243.
[32] R. Zenit, M.L. Hunt, The impulsive motion of a liquid resulting from a particle collision, J. Fluid Mech. 375 (1998) 345–361.
[33] H.J. Pain, The Physics of Vibrations and Waves, fourth ed., Wiley, New York, 1993. pp. 144–163.
[34] P. Pronk, C.A. Infante Ferreira, G.J. Witkamp, Prevention of fouling and scaling in stationary and circulating liquid–solid fluidized bed heat exchangers, ice crystallization fouling, Int. J. Heat Mass Transfer, submitted for publication.
[35] A.G. Duncan, C.D. West, Prevention of incrustation on crystallizer heat-exchangers by ultrasonic vibration, Trans. Inst. Chem. Eng. 50 (1972) 109–114.
[36] M.J. Ashley, Preventing deposition on heat-exchange surfaces with ultrasound, Ultrasonics 12 (1974) 215–221.
[37] P.L. Kaye, C.S.J. Pickles, J.E. Field, K.S. Julian, Investigation of erosion processes as cleaning mechanisms in the removal of thin deposited soils, Wear 186–187 (1995) 413–420.